Physica E 150 (2023) 115705

Contents lists available at ScienceDirect

Physica E: Low-dimensional Systems and Nanostructures

journal homepage: www.elsevier.com/locate/physe

2D Hemiporphyrazine: A new nanoporous material

R.M. Tromer [a,b], M.L. Pereira Júnior [c], L.A. Ribeiro Junior [d,*], D.S. Galvão [a,b]

[a] Applied Physics Department, University of Campinas, Campinas, São Paulo, Brazil
[b] Center for Computing in Engineering and Sciences, University of Campinas, Campinas, São Paulo, Brazil
[c] Department of Electrical Engineering, Faculty of Technology, University of Brasília, Brasília, Brazil
[d] Institute of Physics, University of Brasília, Brasília, Brazil

ARTICLE INFO

Keywords:
Hemiporphyrazine
Two-dimensional materials
Nanoporous material
New 2D material
Density functional theory

ABSTRACT

Crystalline microporous materials are solids formed by interconnected pores of less than 2 nm in size. Typically, they possess large surface areas desirable for versatile applications such as catalysis, gas adsorption, and energy storage. In the present work, we propose a new porphyrin-based 2D nanoporous crystal, named 2D Hemiporphyrazine (2DH), which is formed by topologically assembling $H_5C_{13}N_4$ porphyrins. We have considered its monolayer, bi-layer, and molecular crystal (bulk) arrangements. We carried out DFT calculations to investigate 2DH structural and electronic properties. Results show that 2DH is a very stable structure with a direct bandgap of 0.65 eV and significant optical absorption in the visible range. Simulations also showed the existence of proton transfer between nitrogen atoms. It is the first report on the site-specific hydrogen exchange process in 2D crystals.

1. Introduction

Carbon-based 2D materials, which include graphene as the most important [1,2] and other allotropes [3,4], have been widely investigated to propose new solutions for organic electronics [5–7]. Some graphene properties stand out, such as high thermal and electrical conductivity and mechanical strength [8,9]. However, its null band gap poses some limitations to nanoelectronics since it prevents, for instance, the device from working in the on/off current ratio [10,11].

Strategies for opening the graphene bandgap [12–14] and designing new 2D materials with a semiconducting bandgap in their pristine form have been investigated to overcome this problem [15–17]. Among these new materials, 2D porphyrin-based crystals are attractive due to their small semiconducting band gaps and nanoporous structure with large area surfaces, which are crucial traits for versatile applications such as catalysis [18,19], selectivity [20], gas adsorption [21], and energy storage [22].

Recently, 2D porphyrin-based nanoporous materials have been both experimentally [23–29] and theoretically [30–36] investigated. Abel and coworkers reported the synthesis of a well-ordered organometallic sheet consisting of 2D polymeric phthalocyanine [24]. Phthalocyanine is one of the possible structures that porphyrin molecules can form [37]. The growth demonstrated on a metal surface can be extended onto a thin insulating film. Other 2D porphyrin-based metal–organic frameworks were also successfully synthesized [38–41]. As a general trend, the fabricated materials exhibited good electrocatalytic activity and selectivity.

Density functional theory (DFT) calculations were used to design new 2D porphyrin-based crystals [30–36]. A common feature that can be inferred from these numerical studies, although they are very few in the literature, is that 2D porphyrin-based crystals can present semiconducting electronic bandgaps, ranging between 0.6–2.0 eV [23,31,34]. These bandgap values are in the range required for materials useful in flexible nanoelectronics. In this sense, it is relevant to propose other 2D porphyrin-based crystals to expand understanding of their possible use as active layers in these applications.

In this work, we propose a new porphyrin-based 2D nanoporous crystal (see Fig. 1), named 2D Hemiporphyrazine (2DH), formed by topologically assembling $H_5C_{13}N_4$ porphyrins with four- and six-membered carbon rings. So far, no phthalocyanine species synthesized in crystal form has presented cyclobutane-type rings. Only recently, 2D carbon allotropes with this ring type were synthesized. Examples are the biphenylene network [42], and 2D polymerized fullerenes [43]. The theoretical predictions of these materials preceded their synthesis by decades [44]. We showed that 2DH has good thermal and structural stabilities. Based on that, and in recent synthetic advances mentioned above, 2DH can be synthesized soon.

We used DFT calculations to investigate the structural and electronic properties of 2DH. This material presents a direct bandgap semiconductor with an electronic bandgap value of 0.65 eV and exhibits

* Corresponding author.
E-mail address: ribeirojr@unb.br (L.A. Ribeiro Junior).

https://doi.org/10.1016/j.physe.2023.115705
Received 8 February 2023; Received in revised form 3 March 2023; Accepted 13 March 2023
Available online 20 March 2023

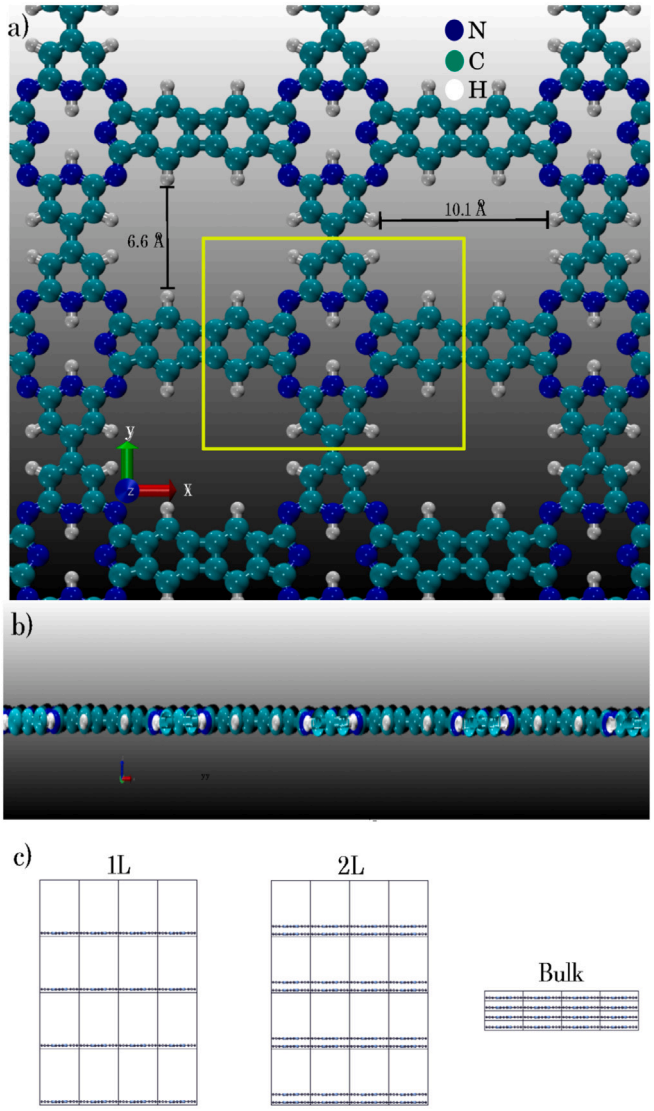

Fig. 1. Schematic representation for the optimized 2DH structure. Its top and side views are presented in (a) and (b), respectively. The color scheme shows the carbon, hydrogen, and nitrogen atoms in cyan, white, and blue, respectively. The yellow region highlights the lattice unit cell, and the red and green arrows illustrate the pore size dimensions along the different directions. Panel (c) shows the supercell configuration for the three 2DH models: (1L) single-layer, (2L) bi-layer, and (Bulk) the molecular crystal. For the 1L and 2L simulations, a vacuum buffer layer of 20 Å was used.

high thermal stability for temperatures up to 2000 K. The absence of negative frequencies in the phonon spectrum confirms its structural stability. Notably, the optical absorption of 2DH is intense within the visible region.

2. Methodology

We performed DFT calculations using the SIESTA code to investigate 2DH electronic and optical properties [45]. We have considered single and bi-layer, as also the molecular crystal (bulk). The simulations were carried out within the generalized gradient approximation (GGA), with the Perdew–Burke–Ernzenhof (PBE) [46,47], as the exchange–correlation functional. We adopted the van der Waals (vdW-DFT) functional of Dion et al. as implemented in the SIESTA code, for treating dispersion effects [48–50]. The norm-conserving Troullier–Martins pseudopotential describes the core electrons [51]. We used two basis sets, double-zeta plus polarization (DZP) and single-zeta (SZ). Sz was used in the AIMD simulations because it has a smaller computational cost.

We used a kinetic energy cut-off of 300 eV. The k-grid is $6 \times 6 \times 1$ for geometry optimization and $30 \times 30 \times 1$ for electronic and optical calculations. A vacuum region of 20 Å is considered to prevent spurious interactions among the 2DH layers. Lattice vectors and atom positions were fully relaxed in the optimization process. The convergence criteria were of maximum force at each atom less than 1.0×10^{-3} eV/Å and for total energy was 1.0×10^{-6} eV. To investigate the structural stability of the 2DH structure, we performed phonon dispersion calculations based on the force constant algorithm for T = 0 K [52].

To obtain the optical properties, we considered an external electric field of 1.0 V/Å along the x and y-directions. This value is characteristic of 2D systems similar to 2DH, such as nitrogenated holey graphene [53]. In this sense, we derived the optical quantities directly from the complex dielectric constant $\epsilon = \epsilon_1 + i\epsilon_2$, where ϵ_1 and ϵ_2 are the real and imaginary parts of dielectric constant, respectively.

From Fermi's golden rule, we obtained the imaginary part of the dielectric constant from the interband optical transitions between valence (VB) and conduction bands (CB),

$$\epsilon_2(\omega) = \frac{4\pi^2}{V_\Omega \omega^2} \sum_{i \in \mathrm{VB},\, j \in \mathrm{CB}} \sum_k W_k \, |\rho_{ij}|^2 \, \delta(\varepsilon_{kj} - \varepsilon_{ki} - \hbar\omega), \tag{1}$$

where ω is the photon frequency, V_Ω the unit cell volume, W_k the k-point weight in the reciprocal space, and ρ_{ij} the dipole transition matrix element [30]. ϵ_1 and ϵ_2 are related through the Kramers–Kronig relation. The real part of the dielectric constant is expressed as:

$$\epsilon_1(\omega) = 1 + \frac{1}{\pi} P \int_0^\infty d\omega' \, \frac{\omega' \epsilon_2(\omega')}{\omega'^2 - \omega^2}, \tag{2}$$

where P is the Cauchy principal value. Once the real and imaginary parts of the dielectric constant are obtained, the other relevant optical coefficients, such as the absorption coefficient α, the refractive index (η), and reflectivity (R), can be derived by:

$$\alpha(\omega) = \sqrt{2}\omega \left[(\epsilon_1^2(\omega) + \epsilon_2^2(\omega))^{1/2} - \epsilon_1(\omega) \right]^{1/2}, \tag{3}$$

$$\eta(\omega) = \frac{1}{\sqrt{2}} \left[(\epsilon_1^2(\omega) + \epsilon_2^2(\omega))^{1/2} + \epsilon_1(\omega) \right]^2, \tag{4}$$

and

$$R(\omega) = \left[\frac{(\epsilon_1(\omega) + i\epsilon_2(\omega))^{1/2} - 1}{(\epsilon_1(\omega) + i\epsilon_2(\omega))^{1/2} + 1} \right]^2. \tag{5}$$

3. Results

3.1. 2DH stability

Simulations performed here start from designing the 2DH structure presented in Fig. 1. The orthorhombic unit cell is highlighted in yellow. It was generated by replacing some C–H with C–C covalent bonds of the hemiporphyrazine molecule previously synthesized [54]. The 2DH single-layer shown in Fig. 1, with composition $H_5C_{13}N_4$, has similar optimized parameters when calculated with both GGA and GGA/vdW approximations, as expected: a = 14.53 Å, b = 11.81 Å, c = 20.00 Å for GGA and a = 14.55 Å, b = 11.80 Å, c = 20.00 for vdW, with $\alpha = \beta = \gamma = 90°$ for both cases. The average bonds are approximately R_{C-C} = 1.44 Å, R_{C-N} = 1.35 Å, R_{N-H} = 1.04 Å and R_{C-H} = 1.10 Å. The distance between atoms within the pore can vary from 6.6 Å to 10.1 Å. Table 1 shows the 2DH lattice parameters, contrasting them with the material's crystalline structure before replacing C–H bonds with C–C bonds at 0 K and 2000 K. The 2DH lattice parameters are similar for both cases.

The 2DH formation enthalpy values are −7.7 and −8.7 eV/atom, obtained with GGA and GGA/vdW, respectively. We also optimized, within GGA/vdW level, the structures corresponding to the cases with

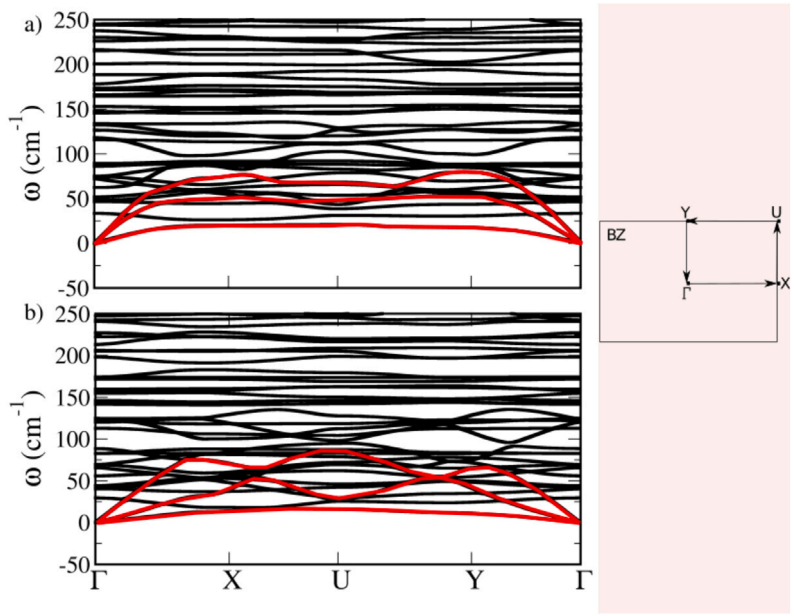

Fig. 2. Phonon dispersion band structure along the high symmetric k-point path in the first Brillouin zone for (a) GGA and (b) GGA/vdW approaches. The high symmetry k-points are: Γ(0.0, 0.0, 0.0), X(0.5, 0.0, 0.0), U(0.5, 0.5, 0.0), Y(0.0, 0.5, 0.0), and Γ(0.0, 0.0, 0.0). We present the acoustic modes in red.

Table 1
a* and b* are the 2DH lattice parameters for the material's crystalline structure before replacing C–H bonds with C–C bonds. p_x and p_y are the average values of the pore diameters in the x and y directions at 0K and 2000 K, respectively.

a*/a (Å)	b*/b (Å)	$\alpha = \beta = \gamma(^o)$	p_x (0K)/p_x (2000K) (Å)	p_y (0K)/p_y (2000K) (Å)
15.32/14.53	12.54/11.81	90	10.10/10.40	6.60/6.80

two infinite layers (molecular crystal). The optimized geometries for these cases remain unchanged when contrasted with the single-layer one, suggesting that the layers do not strongly interact. The interlayer distance is 3.5 Å.

To investigate the 2DH structural stability, we performed phonon dispersion and AIMD calculations. For the phonon dispersion, we considered the following high symmetry k points: $\Gamma \rightarrow X \rightarrow U \rightarrow Y \rightarrow \Gamma$. Fig. 2 shows the phonon dispersion spectra for 2(a) GGA and 2(b) GGA/vdW approximations. In this figure, we notice the absence of negative frequencies, which suggests that the 2DH is stable at T=0 K.

One can also realize that the spectra slightly differ between the two approaches. The acoustic modes close to the Γ point are better described in the GGA/vdW approach since one of the three modes is quadratic, as expected for 2D systems [34]. The first optical mode for GGA and GGA/vdW occurs near 27 cm^{-1}. The three modes are almost horizontal at the Γ point, resulting in lower group velocity. This trend is also expected for 2D systems, in which the acoustic modes are more important for the thermal transport process [55].

We studied the effect of temperature on the 2DH stability using AIMD simulations. Here, we used an NVT ensemble for temperatures up to 2000 K. Fig. 3 shows representative AIMD snapshots for GGA results and a total time of 2 ps. For this AIMD simulation, we replicated the 2DH unit cell 2 times along the x and y-directions. We can notice that in the last snapshot (at 2 ps of simulation), the 2DH structure remains similar to the initial one but presents some buckling caused by the thermal effects. Consequently, we can argue that the 2DH remains stable in high-temperature regimes. We also verified that the 2DH multilayered structures also remain stable but are misaligned with each other (see Supplementary Material).

Another relevant result observed in the AIMD simulations is the proton transfer (site-specific hydrogen exchanges). It occurs when one hydrogen atom, initially bonded to a nitrogen atom, gains sufficient energy to break its bond, forming a new bond with next-neighboring nitrogen. This effect was observed from AIMD simulations when two hydrogen atoms were transferred to their next-neighboring nitrogen site at 0.33 ps, as indicated by the yellow circles in Figs. 3(b) and 3(c). The initial 2DH atomic configuration in Fig. 3(a) differs from the final one in Fig. 3(c), characterizing the proton transfer process. Importantly, this process has been extensively studied in the literature for molecular systems. To our knowledge, this is the first report on the site-specific hydrogen exchange process in 2D crystals.

3.2. 2DH electronic and optical properties

Now, we discuss the electronic and optical properties of the 2DH systems studied here at the GGA/vdW level. Fig. 4 shows the band structure configuration and the corresponding projected density of states (PDOS) for 4(a) single-layer, 4(b) bi-layer, and 4(c) bulk (molecular crystal) cases. It is worth stressing that GGA and GGA/vdW band structures are very similar. For this reason, hereafter, we present only the results using the GGA/vdW approximation.

For the single-layer case (see Fig. 4(a)), 2DH has a direct electronic bandgap of 0.65 eV, close to the Y-point. Moreover, we notice that for the highest occupied crystalline orbital (HOCO), there is a band splitting (0.2 eV) between the X and Y k-points. Besides HOCO, the lowest unoccupied crystalline orbital (LUCO) and other conduction states are predominantly formed by $2p_z$ atomic orbitals of the carbon and nitrogen atoms. In contrast, the states below HOCO are formed by contributions from all orbitals.

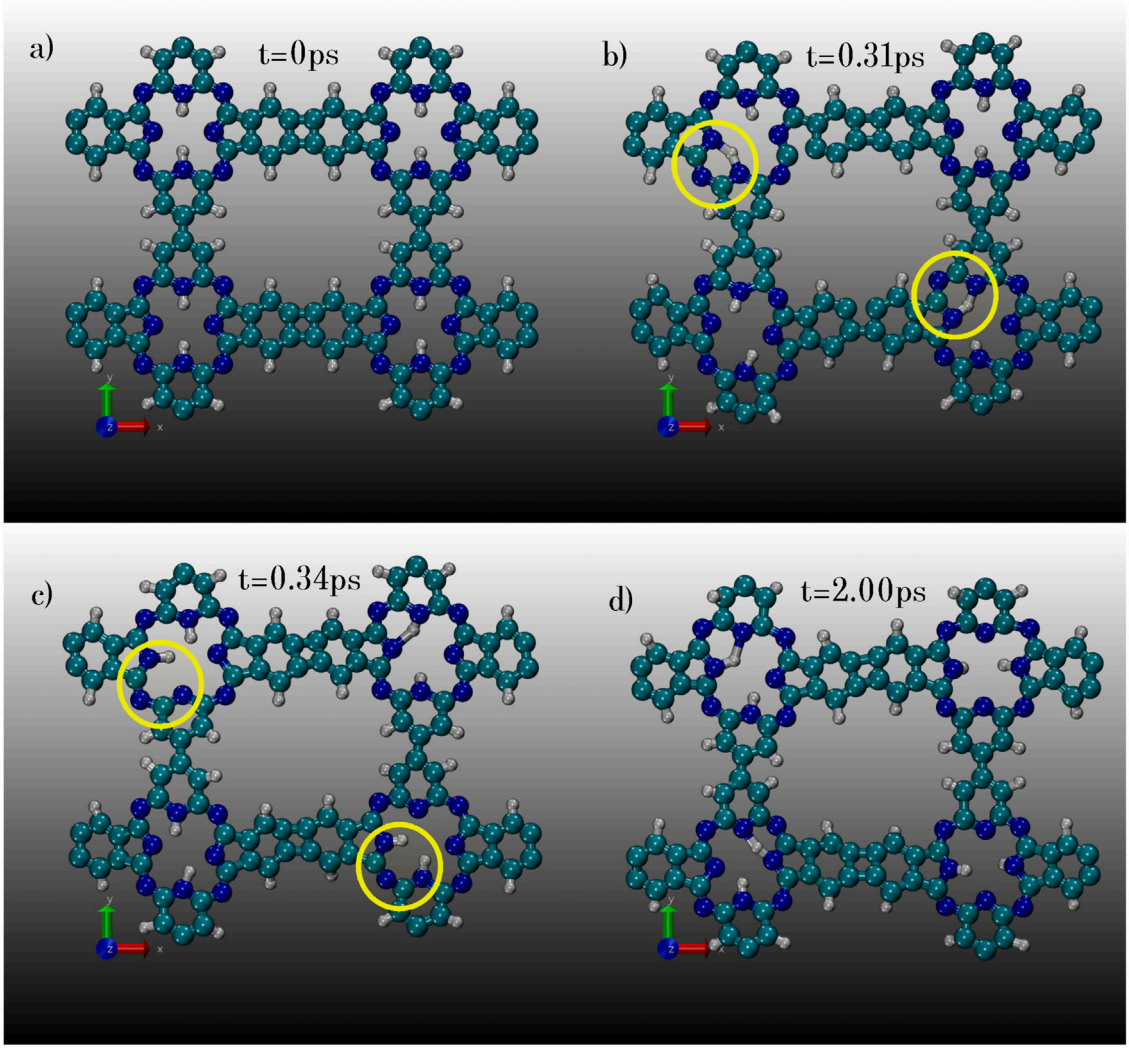

Fig. 3. GGA representative AIMD snapshots for the thermal stability simulation of 2DH at 2000 K. The simulation time increases from (a) to (c) panels. Each panel shows the 2DH lattice configuration at (a) 0.00 ps, (b) 0.33 ps, (c) 2.00 ps, and (d) 2DH side view at 2.00 ps.

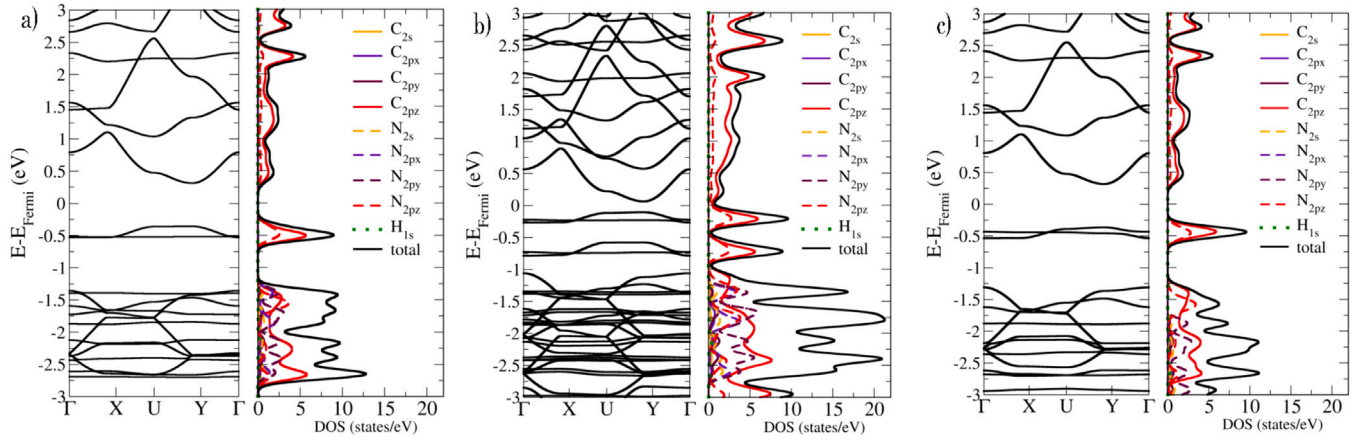

Fig. 4. GGA/vdw electronic band structure and the corresponding Projected Density of States (PDOS) for the 2DH systems in (a) single-layer, (b) bi-layer, and (c) bulk configurations.

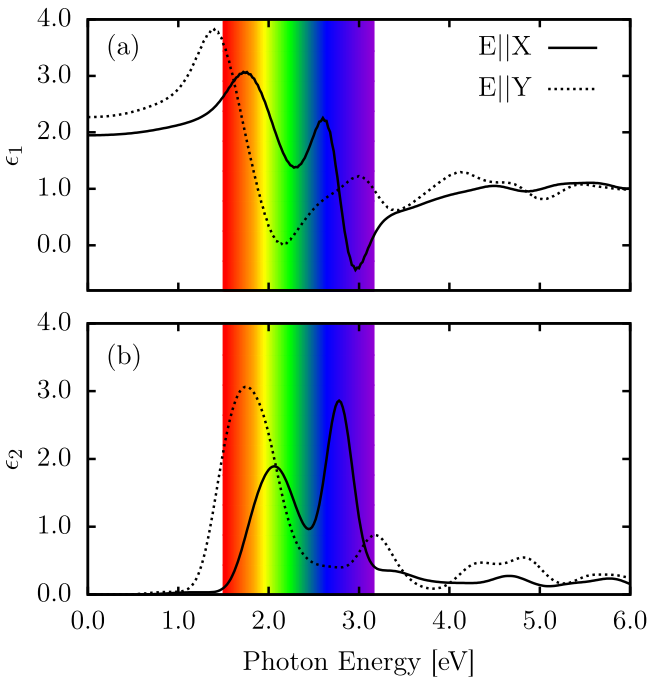

Fig. 5. (a) Real (ϵ_1) and (b) imaginary (ϵ_2) parts of the dielectric constant as a function of photon energy for single-layer 2DH. This figure contrasts the results for ϵ_1 and ϵ_2 considering different orientations for the external electric field.

For the bi-layer case, we can see from Fig. 4(b) that HOCO and HOCO-1 are identical due to the additional layer. The interaction between the layers induces a shift in the valence and conduction states. In this system, the electronic band gap decreases to 0.15 eV, and the corresponding PDOS significantly changes. For the bulk system, we observe that the band structure, and the corresponding PDOS, are very similar to the single-layer case with the electronic bandgap of the bulk phase of 0.66 eV. The same pattern was observed for the LUCO.

In Fig. 5, we present the real (ϵ_1) and imaginary (ϵ_2) parts of the dielectric constant as a function of photon energy when subjected to a polarized external electrical field along the x and y-directions. We also investigated a case where the external electrical field is polarized along the z-direction. This interaction produced very small optical coefficient intensities and is not presented in Fig. 5. The real and imaginary components are associated with dispersive and absorptive optical coefficients. Each peak in the spectrum corresponds to an optical activity between allowed transitions of the electronic states, as shown in Fig. 4.

For ϵ_1, one can see in Fig. 5 that this value is constant for photon energies between 0 and 1 eV. This trend indicates that 2DH does not present optical activity within the infrared range. For photon energies greater than 4 eV, the ϵ_1 value tends to be constant, suggesting a weak optical activity in the violet region. Therefore, the optical activity of single-layer 2DH is more pronounced in the visible range. The X component of the real part of the dielectric function presents negative values for photon energy close to 3 eV. This result indicates that the 2DH layer, when interacting with an external electric field, has a metallic signature [56].

We can also observe that the dispersion trend in the spectra is isotropic along the x and y-directions. The values for static dielectric constant in each direction can be obtained in the long-wavelength limit (when the photon energy drops to zero) [57]. In this sense, $\epsilon_X(0) = 2.0$ and $\epsilon_Y(0) = 2.3$, for the x and y-directions, respectively. For ϵ_2, we notice in Fig. 5 that the optical activity associated with the first interband transitions along the x and y-directions starts for photon energies close to 1.5 and 1.1 eV, respectively. The optical activity occurs with more intensity within the visible region ranging from 1.6 to 3.3 eV.

In Fig. 6, we present the absorption coefficient for 2DH as a function of photon energy for an external electrical field polarized along the x and y-directions. The first allowed optical transitions T_X and T_Y along the x and y-directions, respectively, differ by 0.2 eV. For the sake of clarity, the inset panel in Fig. 6 illustrates the T_X (black) and T_Y (red) transitions in the electronic band structure. These transitions are also highlighted in the absorption coefficient curves as T_X (black bar) and T_Y (red bar) for photon energies of 1.7 and 1.9 eV, respectively. In the two directions of the applied electric field, we notice moderate optical activity within the visible range.

We can explain the difference between the electronic and optical gaps based on the PDOS results since some electronic transitions are not optical allowed due to symmetry constraints. The first optical transitions occur for the crystalline orbitals below the HOCO, as shown in Fig. 6 for T_X and T_Y cases.

Now, we discuss the refractive index (η) and reflectivity (R) for the 2DH as a function of photon energy, as shown in Fig. 7. The η

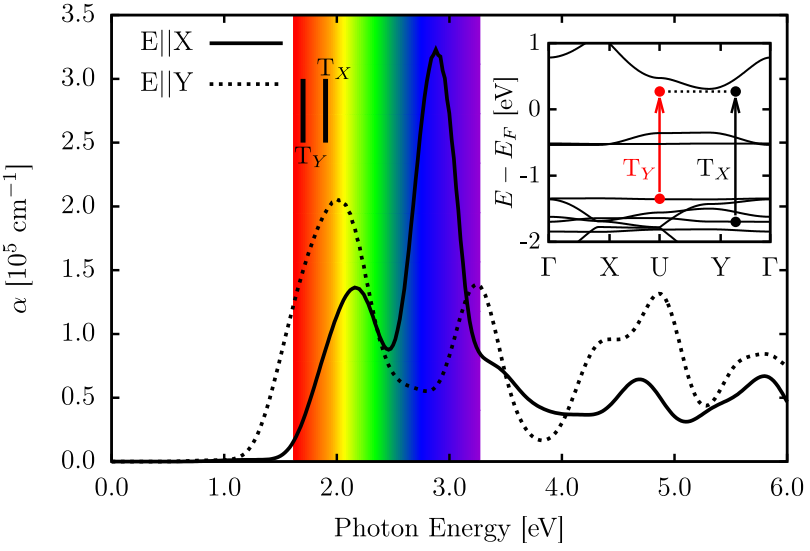

Fig. 6. Absorption coefficient α as a function of photon energy for the 2DH single-layer case. The first allowed optical transitions T_X and T_Y are highlighted in black and red colors, respectively. For clarity, the inset panel illustrates the T_X (black) and T_Y (red) transitions in the electronic band structure.

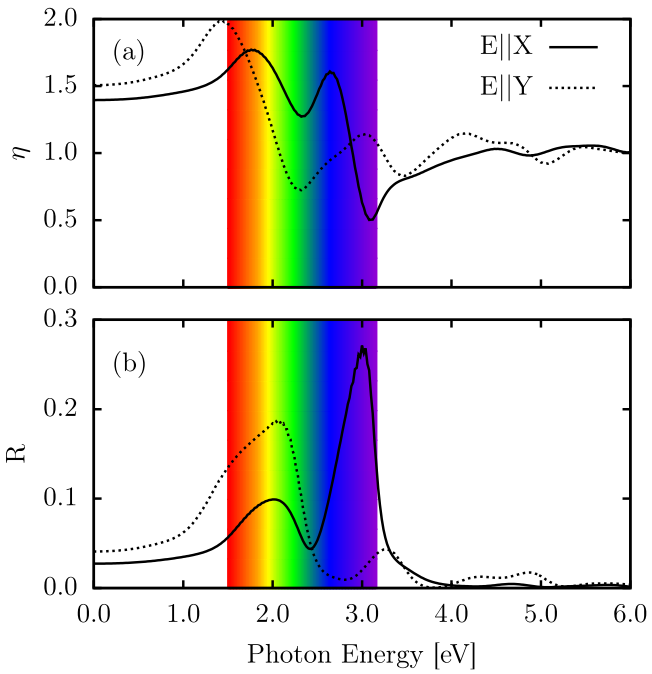

Fig. 7. (a) Refractive index (η) and (b) reflectivity (R) as a function of photon energy for 2DH single-layer.

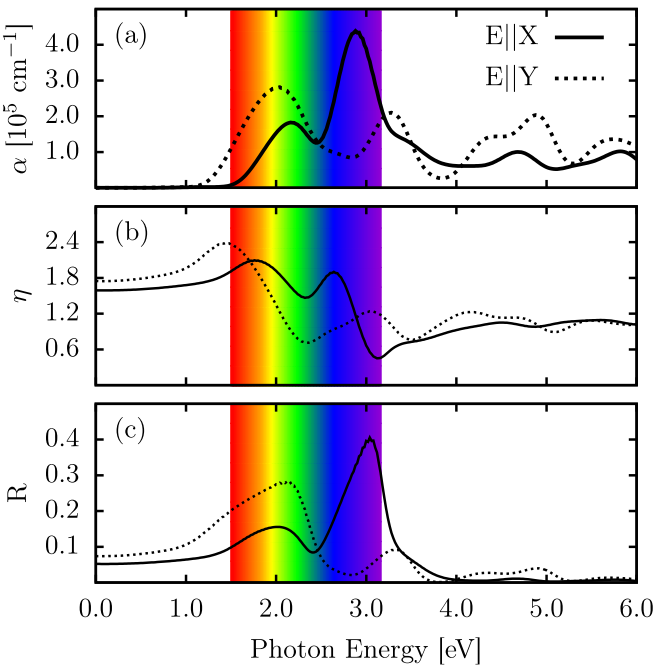

Fig. 8. (a) Absorption coefficient α, (b) Refractive index (η), and (c) reflectivity (R) as a function of photon energy for 2DH double-layer.

index along the x and y-directions is almost constant within the infrared and ultraviolet ranges. We can expect maximum light absorption for photon energies corresponding to the visible region. The maximum refraction occurs near the infrared-visible edge. R also shows more intense activity within the visible region, but the maximum intensity is smaller than 0.3. This value indicates that only 30% of the incident light will be reflected when interacting with 2DH. This feature suggests that 2DH might be helpful in photovoltaic applications.

Finally, we show the optical properties of the double-layer phase (see Fig. 8). The results are similar to the single-layer ones. The difference that we can point out is that, for the single-layer case, the intensity is higher concerning the double-layer phase because the number of allowed states increases with the number of layers, which favors several less intense electronic transitions to occur. Although the electronic bandgap changes in the double-layer case, the optical gap remains unaffected since no new states are present to produce new allowed optical transitions.

4. Conclusions

In summary, we proposed a new porphyrin-based 2D nanoporous structure, named 2D Hemiporphyrazine (2DH), which is formed by topologically assembling $H_5C_{13}N_4$ porphyrins. We considered single, bi-layer, and molecular crystal (bulk) structures.

We carried out DFT calculations to investigate 2DH structural and thermal stability. The 2DH phonon spectrum shows no negative frequencies, suggesting its good structural stability at T=0 K. Temperature effects on the 2DH structural stability were studied using *ab initio molecular dynamics* (AIMD) simulations. The results show structural integrity up at 2000 K.

2DH monolayer has a direct electronic bandgap of 0.65 eV. For the bi-layer case, the electronic band gap decreases to 0.15 eV. For the bulk system, we observed that the band structure, and the corresponding PDOS, are very similar to the single-layer case. The electronic bandgap of the bulk phase is 0.66 eV. 2DH does not present optical activity within the infrared range. Moreover, it has weak optical activity in the violet region, and most light absorption is in the visible spectrum.

Declaration of competing interest

The authors declare the following financial interests/personal relationships which may be considered as potential competing interests: Luiz A. Ribeiro Junior reports financial support was provided by Foundation for Research Support of the Federal District. Douglas S. Galvao reports financial support was provided by State of Sao Paulo Research Foundation. Raphael M. Tromer reports financial support was provided by State of Sao Paulo Research Foundation. Luiz A. Ribeiro Junior reports financial support was provided by National Council for Scientific and Technological Development.

Data availability

No data was used for the research described in the article.

Acknowledgments

This work was financed by the Coordenação de Aperfeiçoamento de Pessoal de Nível Superior (CAPES) - Finance Code 001, Conselho Nacional de Desenvolvimento Cientifico e Tecnológico (CNPq), FAP-DF, and FAPESP. We thank the Center for Computing in Engineering and Sciences at Unicamp for financial support through the FAPESP/CEPID Grants #2013/08293-7 and #2018/11352-7. L.A.R.J acknowledges the financial support from a FAP-DF grants 00193-00000857/2021-14, 00193-00000853/2021-28, 00193.00001808/2022-71, and 00193-00000811/2021-97, and CNPq grants 302922/2021-0 and 350176/2022-1. L.A.R.J. gratefully acknowledges the support from ABIN grant 08/2019 and Fundação de Apoio à Pesquisa (FUNAPE), Edital 02/2022 - Formulário de Inscrição N.4. M.L.P.J. and L.A.R.J. acknowledge Núcleo de Computação de Alto Desempenho (NACAD) and for providing the computational facilities. This work used resources of the Centro Nacional de Processamento de Alto Desempenho em São Paulo (CENAPAD-SP). The authors acknowledge the National Laboratory for Scientific Computing (LNCC/MCTI, Brazil) for providing HPC resources of the SDumont supercomputer, which have contributed to the research results reported within this paper. URL: http://sdumont.lncc.br.

Appendix A. Supplementary data

Supplementary material related to this article can be found online at https://doi.org/10.1016/j.physe.2023.115705.

References

[1] Andre Konstantin Geim, Graphene: status and prospects, Science 324 (5934) (2009) 1530–1534.

[2] Kostya S. Novoselov, Andre K. Geim, Sergei V. Morozov, De-eng Jiang, Yanshui Zhang, Sergey V. Dubonos, Irina V. Grigorieva, Alexandr A. Firsov, Electric field effect in atomically thin carbon films, Science 306 (5696) (2004) 666–669.

[3] Andrey N. Enyashin, Alexander L. Ivanovskii, Graphene allotropes, Phys. Status Solidi (B) 248 (8) (2011) 1879–1883.

[4] Virendra Singh, Daeha Joung, Lei Zhai, Soumen Das, Saiful I. Khondaker, Sudipta Seal, Graphene based materials: past, present and future, Prog. Mater. Sci. 56 (8) (2011) 1178–1271.

[5] Vinay Gupta, Neeraj Chaudhary, Ritu Srivastava, Gauri Datt Sharma, Ramil Bhardwaj, Suresh Chand, Luminscent graphene quantum dots for organic photovoltaic devices, J. Am. Chem. Soc. 133 (26) (2011) 9960–9963.

[6] Tae-Hee Han, Youngbin Lee, Mi-Ri Choi, Seong-Hoon Woo, Sang-Hoon Bae, Byung Hee Hong, Jong-Hyun Ahn, Tae-Woo Lee, Extremely efficient flexible organic light-emitting diodes with modified graphene anode, Nat. Photonics 6 (2) (2012) 105–110.

[7] Frank Schwierz, Graphene transistors, Nature Nanotechnol. 5 (7) (2010) 487–496.

[8] Francesco Bonaccorso, Zhipei Sun, Tawfique Hasan, A.C. Ferrari, Graphene photonics and optoelectronics, Nat. Photonics 4 (9) (2010) 611–622.

[9] Berardi Sensale-Rodriguez, Graphene-based optoelectronics, J. Lightwave Technol. 33 (5) (2015) 1100–1108.

[10] Guanxiong Liu, Sonia Ahsan, Alexander G. Khitun, Roger K. Lake, Alexander A. Balandin, Graphene-based non-Boolean logic circuits, J. Appl. Phys. 114 (15) (2013) 154310.

[11] Jing Ning, Ying Wang, Xin Feng, Boyu Wang, Jianguo Dong, Dong Wang, Chaochao Yan, Xue Shen, Xinran Wang, Jincheng Zhang, et al., Flexible field-effect transistors with a high on/off current ratio based on large-area single-crystal graphene, Carbon 163 (2020) 417–424.

[12] Melinda Y. Han, Barbaros Özyilmaz, Yuanbo Zhang, Philip Kim, Energy band-gap engineering of graphene nanoribbons, Phys. Rev. Lett. 98 (20) (2007) 206805.

[13] Fengnian Xia, Damon B. Farmer, Yu-ming Lin, Phaedon Avouris, Graphene field-effect transistors with high on/off current ratio and large transport band gap at room temperature, Nano Lett. 10 (2) (2010) 715–718.

[14] Emiliano Cadelano, Pier Luca Palla, Stefano Giordano, Luciano Colombo, Elastic properties of hydrogenated graphene, Phys. Rev. B 82 (23) (2010) 235414.

[15] Run-Sen Zhang, Jin-Wu Jiang, The art of designing carbon allotropes, Front. Phys. 14 (1) (2019) 1–17.

[16] Manish Chhowalla, Hyeon Suk Shin, Goki Eda, Lain-Jong Li, Kian Ping Loh, Hua Zhang, The chemistry of two-dimensional layered transition metal dichalcogenide nanosheets, Nature Chem. 5 (4) (2013) 263–275.

[17] B.F. Abrahams, B.F. Hoskins, D.M. Michail, R. Robson, Assembly of porphyrin building blocks into network structures with large channels, Nature 369 (6483) (1994) 727–729.

[18] Wenjing Hao, Dan Chen, Yusen Li, Zongfan Yang, Guolong Xing, Juan Li, Long Chen, Facile synthesis of porphyrin based covalent organic frameworks via an A2B2 monomer for highly efficient heterogeneous catalysis, Chem. Mater. 31 (19) (2019) 8100–8105.

[19] Zhong-Hong Zhu, Yubo Liu, Chi Song, Yating Hu, Guangxue Feng, Ben Zhong Tang, Porphyrin-based two-dimensional layered metal–organic framework with sono-/photocatalytic activity for water decontamination, ACS Nano (2021).

[20] Xuan Zhang, Megan C. Wasson, Mohsen Shayan, Ellan K. Berdichevsky, Joseph Ricardo-Noordberg, Zujhar Singh, Edgar K. Papazyan, Anthony J. Castro, Paola Marino, Zvart Ajoyan, et al., A historical perspective on porphyrin-based metal–organic frameworks and their applications, Coord. Chem. Rev. 429 (2021) 213615.

[21] Nayuesh Sharma, Sandeep Singh Dhankhar, C.M. Nagaraja, A mn (II)-porphyrin based metal-organic framework (MOF) for visible-light-assisted cycloaddition of carbon dioxide with epoxides, Microporous Mesop. Mater. 280 (2019) 372–378.

[22] Huaping Liao, Hongmin Wang, Huimin Ding, Xiangshi Meng, Hai Xu, Baoshan Wang, Xinping Ai, Cheng Wang, A 2D porous porphyrin-based covalent organic framework for sulfur storage in lithium–sulfur batteries, J. Mater. Chem. A 4 (19) (2016) 7416–7421.

[23] Chen Chen, Trinity Joshi, Huifang Li, Anton D. Chavez, Zahra Pedramrazi, Pei-Nian Liu, Hong Li, William R. Dichtel, Jean-Luc Bredas, Michael F. Crommie, Local electronic structure of a single-layer porphyrin-containing covalent organic framework, ACS Nano 12 (1) (2018) 385–391.

[24] Mathieu Abel, Sylvain Clair, Oualid Ourdjini, Mireille Mossoyan, Louis Porte, Single layer of polymeric Fe-phthalocyanine: an organometallic sheet on metal and thin insulating film, J. Am. Chem. Soc. 133 (5) (2011) 1203–1205.

[25] Wei Yang, Bin Li, Hailong Wang, Osamah Alduhaish, Khalid Alfooty, Mohie Aldin Zayed, Peng Li, Hadi D. Arman, Banglin Chen, A microporous porphyrin-based hydrogen-bonded organic framework for gas separation, Cryst. Growth Des. 15 (4) (2015) 2000–2004.

[26] Zengqi Zhang, Jun Li, Yahong Yao, Shu Sun, Permanently porous Co (II) porphyrin-based hydrogen bonded framework for gas adsorption and catalysis, Cryst. Growth Des. 15 (10) (2015) 5028–5033.

[27] Xiaoyi Xu, Shizhao Wang, Yan Yue, Ning Huang, Semiconductive porphyrin-based covalent organic frameworks for sensitive near-infrared detection, ACS Appl. Mater. Interfaces 12 (33) (2020) 37427–37434.

[28] Subhajit Bhunia, Sabuj Kanti Das, Rajkumar Jana, Sebastian C. Peter, Santanu Bhattacharya, Matthew Addicoat, Asim Bhaumik, Anirban Pradhan, Electrochemical stimuli-driven facile metal-free hydrogen evolution from pyrene-porphyrin-based crystalline covalent organic framework, ACS Appl. Mater. Interfaces 9 (28) (2017) 23843–23851.

[29] Hatem M. Titi, Bharat Kumar Tripuramallu, Israel Goldberg, Porphyrin-based assemblies directed by non-covalent interactions: highlights of recent investigations, CrystEngComm 18 (19) (2016) 3318–3339.

[30] Raphael M. Tromer, Leonardo D. Machado, Cristiano F. Woellner, Douglas S. Galvao, Thiophene-tetrathia-annulene monolayer (TTA-2D): A new 2D semiconductor material with indirect bandgap, Physica E 129 (2021) 114586.

[31] Bhaskar Chilukuri, Ursula Mazur, K.W. Hipps, Structure, properties, and reactivity of porphyrins on surfaces and nanostructures with periodic DFT calculations, Appl. Sci. 10 (3) (2020) 740.

[32] Sharani Roy, Christopher B. George, Mark A. Ratner, Catalysis by a zinc-porphyrin-based metal–organic framework: from theory to computational design, J. Phys. Chem. C 116 (44) (2012) 23494–23502.

[33] Gan Luo, Yu Wang, Yafei Li, Two-dimensional iron-porphyrin sheet as a promising catalyst for oxygen reduction reaction: a computational study, Science Bulletin 62 (19) (2017) 1337–1343.

[34] Raphael M. Tromer, Isaac M. Felix, Aliliane Freitas, Sérgio Azevedo, Luiz Felipe C. Pereira, Diboron-porphyrin monolayer: A new 2D semiconductor, Comput. Mater. Sci. 172 (2020) 109338, URL https://www.sciencedirect.com/science/article/pii/S0927025619306378.

[35] Said Hamad, Norge C. Hernandez, Alex Aziz, A. Rabdel Ruiz-Salvador, Sofia Calero, Ricardo Grau-Crespo, Electronic structure of porphyrin-based metal–organic frameworks and their suitability for solar fuel production photocatalysis, J. Mater. Chem. A 3 (46) (2015) 23458–23465.

[36] Harish K. Singh, Pawan Kumar, Umesh V. Waghmare, Theoretical prediction of a stable 2D crystal of vanadium porphyrin: A half-metallic ferromagnet, J. Phys. Chem. C 119 (45) (2015) 25657–25662.

[37] Israel Goldberg, Crystal engineering of porphyrin framework solids, Chem. Commun. (10) (2005) 1243–1254.

[38] Shuanglong Lu, Yiming Hu, Shun Wan, Ryan McCaffrey, Yinghua Jin, Hongwei Gu, Wei Zhang, Synthesis of ultrafine and highly dispersed metal nanoparticles confined in a thioether-containing covalent organic framework and their catalytic applications, J. Am. Chem. Soc. 139 (47) (2017) 17082–17088.

[39] Rufan Chen, Yang Wang, Yuan Ma, Arindam Mal, Xiao-Ya Gao, Lei Gao, Lijie Qiao, Xu-Bing Li, Li-Zhu Wu, Cheng Wang, Rational design of isostructural 2D porphyrin-based covalent organic frameworks for tunable photocatalytic hydrogen evolution, Nature Commun. 12 (1) (2021) 1–9.

[40] Yue Zhou, Lirong Zheng, Deren Yang, Haozhou Yang, Qichen Lu, Qinghua Zhang, Lin Gu, Xun Wang, Enhancing CO2 electrocatalysis on 2D porphyrin-based metal–organic framework nanosheets coupled with visible-light, Small Methods 5 (2) (2021) 2000991.

[41] Yuewu Zhao, Ling Jiang, Li Shangguan, Li Mi, Anran Liu, Songqin Liu, Synthesis of porphyrin-based two-dimensional metal–organic framework nanodisk with small size and few layers, J. Mater. Chem. A 6 (6) (2018) 2828–2833.

[42] Qitang Fan, Linghao Yan, Matthias W. Tripp, Ondřej Krejčí, Stavrina Dimosthenous, Stefan R. Kachel, Mengyi Chen, Adam S. Foster, Ulrich Koert, Peter Liljeroth, J. Michael Gottfried, Biphenylene network: A nonbenzenoid carbon allotrope, Science 372 (6544) (2021) 852–856.

[43] Lingxiang Hou, Xueping Cui, Bo Guan, Shaozhi Wang, Ruian Li, Yunqi Liu, Daoben Zhu, Jian Zheng, Synthesis of a monolayer fullerene network, Nature 606 (7914) (2022) 507–510.

[44] Savas Berber, Eiji Osawa, David Tománek, Rigid crystalline phases of polymerized fullerenes, Phys. Rev. B 70 (8) (2004) 085417.

[45] José M. Soler, Emilio Artacho, Julian D. Gale, Alberto García, Javier Junquera, Pablo Ordejón, Daniel Sánchez-Portal, The SIESTA method for ab initio order-n materials simulation, J. Phys.: Condens. Matter 14 (11) (2002) 2745.

[46] John P. Perdew, Kieron Burke, Matthias Ernzerhof, Generalized gradient approximation made simple, Phys. Rev. Lett. 77 (18) (1996) 3865.

[47] Matthias Ernzerhof, Gustavo E. Scuseria, Assessment of the Perdew–Burke–Ernzerhof exchange-correlation functional, J. Chem. Phys. 110 (11) (1999) 5029–5036.

[48] M. Dion, H. Rydberg, E. Schröder, D.C. Langreth, B.I. Lundqvist, Van der Waals density functional for general geometries, Phys. Rev. Lett. 92 (24) (2004) 246401.

[49] T. Thonhauser, Valentino R. Cooper, Shen Li, Aaron Puzder, Per Hyldgaard, David C. Langreth, Van der Waals density functional: Self-consistent potential and the nature of the van der Waals bond, Phys. Rev. B 76 (12) (2007) 125112, URL https://link.aps.org/doi/10.1103/PhysRevB.76.125112.

[50] Guillermo Román-Pérez, José M. Soler, Efficient implementation of a van der Waals density functional: Application to double-wall carbon nanotubes, Phys. Rev. Lett. 103 (9) (2009) 096102, URL https://link.aps.org/doi/10.1103/PhysRevLett.103.096102.

[51] N. Troullier, José Luís Martins, Efficient pseudopotentials for plane-wave calculations, Phys. Rev. B 43 (1991) 1993–2006.

[52] Brent Fultz, Vibrational thermodynamics of materials, Prog. Mater. Sci. 55 (4) (2010) 247–352, URL https://www.sciencedirect.com/science/article/pii/S0079642509000577.

[53] Raphael M. Tromer, Marcos G.E. da Luz, Mauro S. Ferreira, Luiz Felipe C. Pereira, Atomic adsorption on nitrogenated holey graphene, J. Phys. Chem. C 121 (5) (2017) 3055–3061.

[54] E. Agostinelli, D. Attanasio, I. Collamati, V. Fares, Hemiporphyrazine, a porphyrin-related macrocycle that induces rhombically compressed stereochemistries: structure and properties of bis(pyridine)(hemiporphyrazinato)nickel(II), Inorg. Chem. 23 (8) (1984) 1162–1165.

[55] Alexander A. Balandin, Denis L. Nika, Phononics in low-dimensional materials, Mater. Today 15 (6) (2012) 266–275, URL https://www.sciencedirect.com/science/article/pii/S1369702112701177.

[56] A. Alù, A. Salandrino, N. Engheta, Negative effective permeability and left-handed materials at optical frequencies, Opt. Express 14 (4) (2006) 1557–1567, URL http://opg.optica.org/oe/abstract.cfm?URI=oe-14-4-1557.

[57] Raphael M. Tromer, Levi C. Felix, Cristiano F. Woellner, Douglas S. Galvao, A DFT investigation of the electronic, optical, and thermoelectric properties of pentadiamond, Chem. Phys. Lett. 763 (2021) 138210, URL https://www.sciencedirect.com/science/article/pii/S0009261420311143.